PHYSICAL REVIEW B **99**, 195303 (2019)

Shape effect on the valley splitting in lead selenide nanowires

I. D. Avdeev[*]
Ioffe Institute, Saint Petersburg 194021, Russia

(Received 11 February 2019; revised manuscript received 2 April 2019; published 13 May 2019)

We study the cross-section shape and size effects on the valley splitting in PbSe nanowires within the framework of empirical $sp^3d^5s^*$ tight-binding method. We consider idealized prismatic nanowires, grown along [110], with the cross-section shape varying from rectangular (terminated by {001} and {110} facets) to rhombic (terminated mostly by {111} facets). The valley splitting energies have the maximal value (up to hundreds of meV) in rectangular nanowires, while in rhombic ones they are almost absent. The shape dependence is shown to be similar in nanowires with different point symmetry in a wide range of cross-section sizes.

DOI: 10.1103/PhysRevB.99.195303

I. INTRODUCTION

Lead chalcogenide nanowires (NWs) have a wide range of possible applications. They can be used as circuit components [1,2] and as light emitting (detecting) [3,4] and energy harvesting [5,6] devices. Throughout the past decades a big effort has been made towards experimental NW growth techniques [7–12]. They include colloidal synthesis [10], solution-liquid-solid [12] methods, and even oriented attachment of lead salt nanocrystals [8]. Nowadays it is not only possible to grow a nanowire a few nanometers thin [13] but also to control its shape [14–16], size [17], and growth direction [18]. Nonetheless, theoretical modeling of lead chalcogenide NWs is quite challenging due to the multivalley band structure and strong intervalley coupling in these systems. It was shown [19] that the valley splitting can exceed the excitonic exchange splitting, so the study of the valley splitting is very important to understand the fundamental electronic and optical properties of PbSe NWs.

Lead selenide is a narrow direct band-gap semiconductor (0.17 eV [20]) with the band extrema located at four inequivalent L valleys. In bulk crystal the ground electron and hole states are eightfold degenerate by spin and valley degree of freedom, while in NWs this degeneracy is removed. There are two main mechanisms that split the valley multiplets (sets of confined states originated from different valleys) in PbSe NWs: the mass anisotropy [21] and the intervalley coupling [22] at the NW surface [23]. The first one is readily incorporated in the $\boldsymbol{k}\cdot\boldsymbol{p}$ and splits the valley multiplets in NWs only partially [21]. The second one fully removes the valley degeneracy and can be included in the $\boldsymbol{k}\cdot\boldsymbol{p}$ phenomenologically [23], but for careful theoretical description it requires an atomistic approach [24,25] as it is very sensitive to the microscopic structure of the NW [26,27].

It was shown [27] for cylindrical PbSe NWs and spherical quantum dots [26] that the valley splitting depends on diameter and the point symmetry of the considered structure. In this paper we also take the shape of the NW into account. Following the theoretical [28,29] and experimental [8] data, PbSe nanowires tend to have faceted structure, therefore instead of cylindrical it is more convenient to consider prismatic shape of the NWs. For simplicity we consider idealized prismatic wires, carved out from ideal bulk PbSe crystal. With this approach, the microscopic structure of NWs is fully determined by the cross section and the spatial orientation of the covering prism. Even though the most natural growth direction of PbSe NWs is [001] [8], we consider [110] as the growth direction for the following reason: along this axis the two pairs of the L valleys remain inequivalent [25] which allows us to explicitly evaluate the valley splitting energies for each pair and study their dependencies on the NW shape parameters.

Among many atomistic methods we chose the empirical tight-binding approach in nearest-neighbor approximation, proved to be useful for many cubic semiconductors [30]. The use of the recent parametrization [26], which accurately reproduces experimental effective masses in the L valleys and shows good agreement with experiment [31], allows us to study a wide range of NW sizes and shapes. We neglect the surface passivation, as the surface states in highly ionic crystals lie far outside the band gap [22] and there is no need to saturate the dangling bonds [25]. Note, even though the *ab initio* methods, such as DFT [32,33] and GW [34,35], are more accurate, complexity and demand in computational power make them hardly applicable to relatively large structures (more than a few hundred atoms).

In this paper we show that the valley splitting drastically depends on the NW shape. The valley splitting is almost absent in NWs with the surface terminated mostly by {111} facets and has the maximal value in NWs with {110} and {001} terminated surfaces. We also notice that these are the most stable PbSe surfaces [28,29]. Despite the polar nature, the {111} facets are also present in real systems, especially in colloidal solvents, where they can be passivated by ligands [33,36].

II. VALLEY COUPLING IN NANOWIRES

The structure of the valley splittings is easier to analyze using the perturbative approach [23]. Without the valley

---

[*] ivan.avdeev@mail.ioffe.ru

©2019 American Physical Society

coupling all the L valleys are independent and their energy spectra are fully determined by mass anisotropy [21] and quantum confinement [37]. The latter we associate with a set of quantum numbers q, well established for cylindrical PbSe nanowires [27]. It is important that sets of states with a certain q (valley multiplets) are well distinguishable in the tight binding [27,38,39], where we consider the abrupt NW boundary as a perturbation that mixes the valley states.

For further discussion, we enumerate the L valleys and corresponding wave vectors $\boldsymbol{k}$ by index $\mu \in \{0, 1, 2, 3\}$:

$$\boldsymbol{k}_0 = \frac{\pi}{a}(1, \quad 1, \quad 1), \quad \boldsymbol{k}_1 = \frac{\pi}{a}(-1, -1, \quad 1),$$
$$\boldsymbol{k}_2 = \frac{\pi}{a}(1, -1, -1), \quad \boldsymbol{k}_3 = \frac{\pi}{a}(-1, \quad 1, -1), \qquad (1)$$

where a is the lattice constant. In idealized NWs with translation period $\boldsymbol{T} = a(1, 1, 0)/2$ two of the valleys, L_0 and L_1, project on the NW axis to the edge of the NW's Brillouin zone ($k = \pi/T$), while the others, L_2 and L_3, project to the Γ point ($k = 0$) [25]. Therefore $L_0 \to L_1$ and $L_2 \to L_3$ intervalley scattering processes are independent. Hence the valley splitting can be described by a simple 2×2 Hamiltonian:

$$H_{\text{valley}} = \begin{pmatrix} E_\mu & M_{\mu,\nu} \\ M_{\nu,\mu} & E_\nu \end{pmatrix}, \quad \mu, \nu = 0, 1 \text{ or } 2, 3. \qquad (2)$$

Here $E_\mu = E_\nu$, since the mass anisotropy does not contribute ($m_0^* = m_1^*$ and $m_2^* = m_3^*$ with respect to the NW axis [21]), and $M_{\mu,\nu} = M_{\nu,\mu}^*$ describes the intervalley scattering at the NW surface. Following Ref. [26] one may estimate $M_{\mu,\nu}$:

$$M_{\mu,\nu} = C \sum_n e^{-i(\boldsymbol{k}_\mu - \boldsymbol{k}_\nu)\boldsymbol{R}_n} \Phi_\mu^*(\boldsymbol{R}_n)\Phi_\nu(\boldsymbol{R}_n), \qquad (3)$$

where Φ is an envelope function, $\boldsymbol{R}_n$ is a lattice node, and C is a microscopic constant, given by integral over the primitive cell. Despite the deceptive simplicity, evaluation of the matrix element is difficult as one has to compute the microscopic constant and exact envelopes and deal with the spin degeneracy. The spin cannot be excluded due to its strong influence on the PbSe band structure. Equation (3), however, helps to compare the two $L_0 \to L_1$ and $L_2 \to L_3$ scattering processes. One can show that the phase factors, $e^{-i(\boldsymbol{k}_0 - \boldsymbol{k}_1)\boldsymbol{R}_n}$ and $e^{-i(\boldsymbol{k}_2 - \boldsymbol{k}_3)\boldsymbol{R}_n}$, are the same, which assumes similar dependencies of the valley splitting on the microscopic NW structure.

For numerical simulations we use the supercell approach [40]. We control the structure of NW supercells by four integers: size parameter $N > 0$, shape parameter M ($0 \leqslant M \leqslant N$), and two additional numbers $dN_1, dN_2 \in \{0, 1\}$ to adjust the NW symmetry. The NW supercells are prepared in two steps: first we make a parallelepiped consisting of $(2N + 2 + dN_1) \times (2N + 1 + dN_2)$ atomic layers along the $[\bar{1}10]$ and [001] directions. Due to the periodicity, the supercells are only two atomic layers thick along the translation vector $\boldsymbol{T}$. Then we form the NW shape by cutting M {111} atomic layers from the corners of the parallelepiped along $[1\bar{1}1]$ and $[\bar{1}11]$ directions, as shown in Fig. 1. Below we will refer to the NWs with the shape parameter $M = 0$ as "rectangular" and the ones with $M = N$ as "rhombic."

In total we consider four different NW types and five different atomic configurations. The first NW type has D_{2h} symmetry and two possible atomic configurations: I, cation centered, and Ia, anion centered. The second and the third NW types have C_{2v} symmetry. The last, IV NW type, has C_{2h} symmetry with nonsymmorphic spatial group. All the NW types and their atomic configurations (with $N = 0$) are summarized in Table I. Note that NWs of type II and III have different orientation of C_2 axes. More detail on the NW symmetry is given in Appendix A.

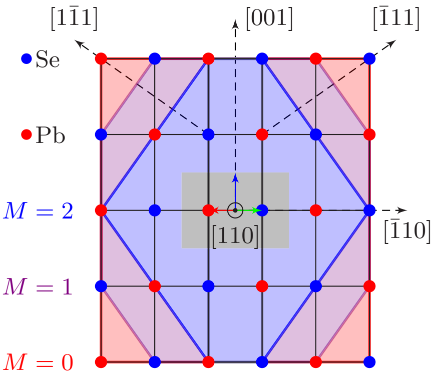

FIG. 1. [110] view onto the NW supercells of type II with size parameter $N = 2$ and different shape parameters M. The supercells with $M = 0, 1, 2$ are enclosed in red (rectangular), violet, and blue (rhombic) regions. The gray region in the middle corresponds to the smallest possible supercell of type II, shown also in Table I. The small RGB arrows show the xyz crystallographic axes.

III. RESULTS AND DISCUSSION

In this paper we focus on NWs of intermediate size, where the valley splittings are large enough and the NWs are not too small. It was shown [27] that the valley splitting becomes negligible (compared to exchange energy [19]) in relatively large systems and is the most pronounced in wires with diameters $\lesssim$50 Å. Below we show the data for NWs with size parameters $2 \leqslant N \leqslant 9$ corresponding to the range of the NW cross-section sizes from $\approx$10 to $\approx$50 Å.

Regarding the symmetry, the first three types of NWs are simple. Indeed, the only spinor representations of D_{2h} (I, Ia) and C_{2v} (II, III) are two-dimensional $\Gamma_5^\pm$ and Γ_5, respectively [41]. This justifies the simple model, Eq. (2), which allows us to unambiguously relate the splitting energy with the intervalley scattering matrix element as $\Delta E = 2|M|$. In the D_{2h} NWs, with the inversion center at the cation (anion), consecutive valley multiplets have opposite parity, therefore the valley multiplets are split via self-scattering at the NW surface. In

TABLE I. Four considered NW types and their smallest supercells ($N = 0$). The cation, located at (0,0,0) in the bulk coordinates frame, is marked with "x." ●, Pb; ●, Se (for Ia only: ●, Se; ●, Pb).

		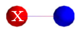	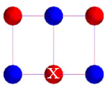	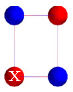
NW type	I, Ia	II	III	IV
Symmetry	D_{2h}	C_{2v}	C_{2v}	C_{2h}
dN_1, dN_2	1, 0	0, 0	1, 1	0, 1

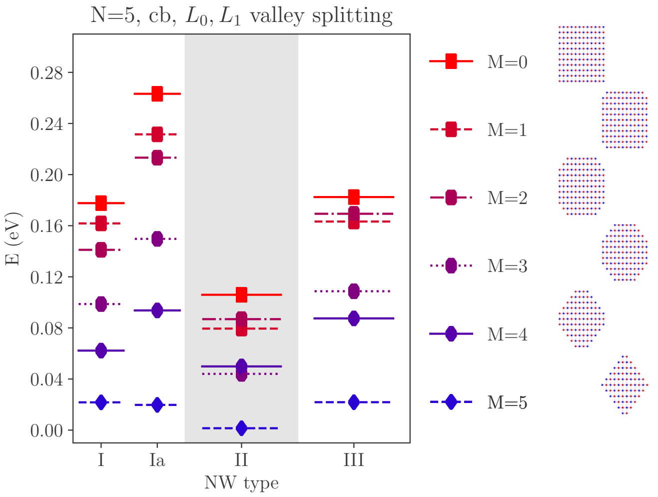

FIG. 2. Valley splitting energies of the L_0, L_1 ground conduction multiplet in NWs of types I, II, and III with the size parameter $N = 5$ as a function of the shape parameter M. Corresponding NW supercells (of type II) are shown on the right with atomic resolution.

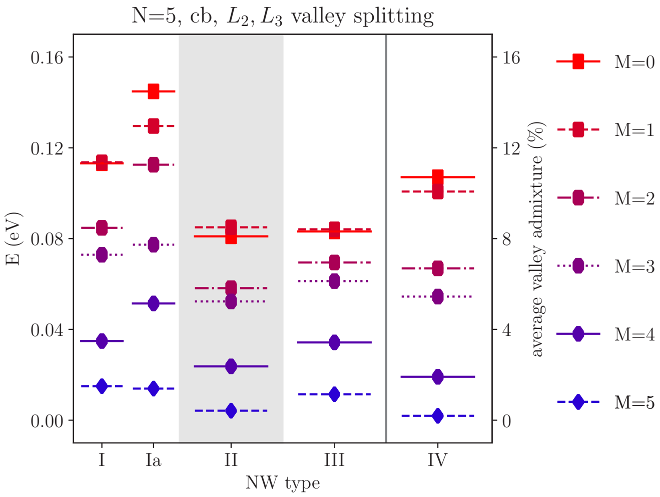

FIG. 3. NWs of type I, II, and III: the same as in Fig. 2, but for the L_2, L_3 ground conduction multiplet. NWs of type IV: relative average valley admixture, $(\Delta\rho_2 + \Delta\rho_3)/2$, in NWs with the size parameter $N = 5$ as a function of the shape parameter M.

the C_{2v} NWs, the lack of spatial inversion also allows for the valley coupling with high-energy multiplets, though this is assumed to be negligible. In the C_{2h} NWs (type IV), the spatial symmetry forbids the splitting of the L_0, L_1 multiplets and the main mechanism of the L_2, L_3 valley splitting becomes the coupling with high-energy states. Detailed analysis of this case is given below and in Appendix B.

In Fig. 2 we show the valley splitting energies of the L_0, L_1 ground conduction multiplet as a function of the shape parameter M in NWs of the first three types (see Table I) with the shape parameter $N = 5$ (the approximate lateral size of NWs is 25×30 Å). The valley splittings are maximal in rectangular NWs ($M = 0$), which have surfaces terminated by $\{001\}$ and $\{110\}$ facets. Particularly strong splittings are in nonstoichiometric anion centered NWs (type Ia). In rhombic NWs ($M = N$) the valley splittings are strongly suppressed (about an order of magnitude). These NWs have surfaces mostly covered by $\{111\}$ facets. Even though the $\{111\}$ facets of PbSe are polar and structurally unstable [29], their stability can be recovered by passivation [28,42]. Therefore we assume that neglecting the built-in electric field from polar facets is a reasonable approximation. Note that the NWs of type III have one extra $(\bar{1}10)$ and one extra (001) atomic planes compared to the NWs of type II, but their splitting energies of the ground L_0, L_1 multiplet are almost twice as large. The same applies for NWs of type I and Ia. NWs of type IV are not shown here, as in this case the L_0, L_1 valley multiplet acquires an extra degeneracy due to the time-reversal symmetry (see Appendix B). In the valence band the valley splittings have similar shape dependence and comparable absolute values, with the exception of NW type I, where, due to the nonstoichiometric origin, the valley splittings in the valence band are strongly suppressed, especially for L_2, L_3 valleys.

The valley splitting energies of the L_2, L_3 ground conduction multiplet as a function of the shape parameter M in NWs with $N = 5$ are summarized in Fig. 3. They are only about two-thirds of the corresponding splittings of the L_0, L_1 multiplet, which is mostly due to the mass anisotropy. Indeed, the L_2 and L_3 valleys lie within the (110) plane, while the L_0 and L_1 are tilted towards the wire axis and therefore have lighter effective in-plane masses [see Eq. (A2)]. Also note that there is almost no difference in the splitting energies between NWs of type II and III.

Now let us turn to the NWs of type IV, shown in the right column in Fig. 3. In these NWs the L_2 and L_3 ground valley multiplet is split via a completely different mechanism. Since the inversion center in NWs of type IV is located between atoms (see Table I), the L_2 and L_3 valleys have different parity and cannot mix directly. The parity of an L_μ valley is related to phase factors $e^{i\boldsymbol{k}_\mu \boldsymbol{R}}$ at lattice nodes. For $\boldsymbol{R} = \pm a(0, 1, 1)/4$, positions of the two closest to inversion center cations, these phases are $\mp i$ for the L_2 valley and 1 for the L_3 valley. This implies that the L_2 (L_3) valley is odd (even) and that the valley coupling in this case is only possible via far energy states.

In fact, this possibility is realized and is the most pronounced in rectangular NWs (shape parameter $M = 0$), similarly to the valley splittings. To illustrate this, in Fig. 4 we show the local density of states in reciprocal space (kLDOS,

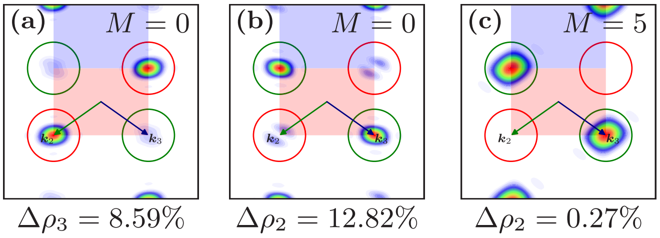

$\Delta\rho_3 = 8.59\%$ $\Delta\rho_2 = 12.82\%$ $\Delta\rho_2 = 0.27\%$

FIG. 4. kLDOS of the L_2, L_3 ground conduction multiplet states in NWs of the type IV. (a) Admixture of the L_2 valley state to the L_3 valley state in the rectangular NW. (b) Admixture of L_3 to L_2 in the rectangular NW and (c) the same in the rhombic NW. Red (green) circles show the area used to estimate the local density $\rho_{2(3)}$ near the $L_{2(3)}$ valley. The size parameter $N = 5$.

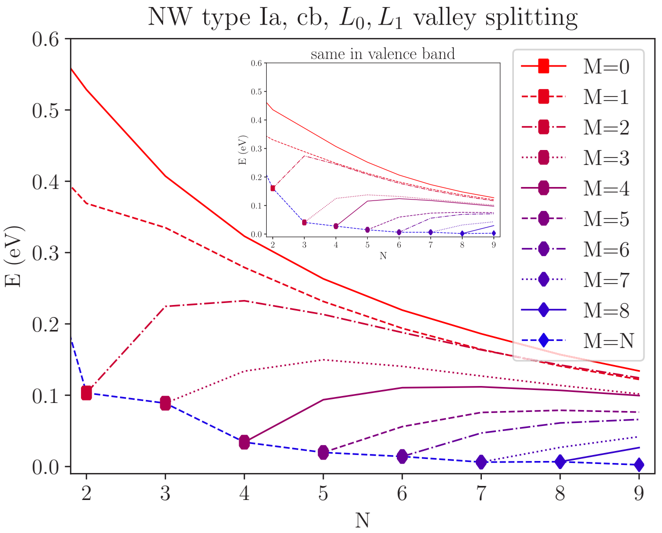

FIG. 5. The valley splitting energies of the L_0, L_1 ground conduction multiplet in NWs of type Ia as a function of the NW shape (M) and size (N) parameters. Lines connect data points with the same M. Each line starts from $N = M$ (indicated by a marker) and has a unique combination of color and style. Inset: Same splittings in the valence band.

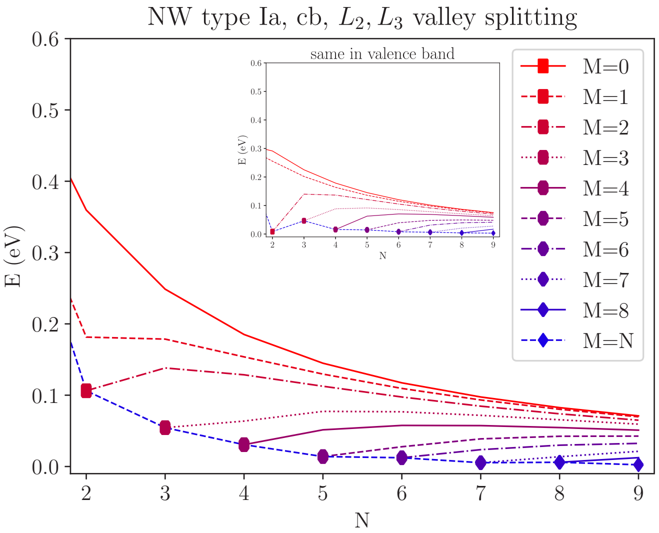

FIG. 6. Same as in Fig. 5, but for L_2, L_3 multiplets.

see Refs. [27,43] for details). For quantitative description of the valley coupling we introduce "valley admixture":

$$\Delta\rho_{2(3)} = \frac{\rho_{2(3)}}{\rho_2 + \rho_3}, \tag{4}$$

where $\rho_{2(3)}$ is the valley density, integrated over a small region near the L_2 (L_3) valley shown by red (green) circles in Fig. 4. One can see that the valley admixture in rectangular NWs is much higher that in rhombic ones. The value $\Delta\rho_3$ in rhombic NWs ($M = N = 5$) is 0.11% and the corresponding kLDOS is not shown in Fig. 4. The density distributions near the main peaks in Figs. 4(a)–4(c) are s-like (corresponding to the ground multiplet), while distributions near the secondary peaks in Figs. 4(a) and 4(b) are d- and p-like, respectively. This proves that the admixed states belong to different valley multiplets. Note, for convenience in Fig. 3 we show the average valley admixtures $(\Delta\rho_2 + \Delta\rho_3)/2$ for the NWs of type IV.

Previously, we discussed NWs with the size parameter $N = 5$ (ten atomic layers along the [001] and [$\bar{1}$10] directions). Next, in Figs. 5 and 6 we show both size (N) and shape (M) dependencies of the valley splittings in conduction and valence bands. We show the data only for the anion centered NWs of type Ia, where the splittings are the most pronounced. We vary the size parameter N from 2 to 9 so the lateral size of NWs changes from 13×12 to 43×55 Å^2 along the [$\bar{1}$10] and [001] axes, respectively. In order to highlight the shape and size dependencies, in Figs. 5 and 6 we connect data points with the same parameter M by color lines (solid red for $M = 0$, dashed blue for $M = N$). For each size parameter N, the shape parameter M satisfies $0 \leqslant M \leqslant N$, therefore each line in Figs. 5 and 6 starts from $N = M$. The starting point of each line (except for $M = 0$ and $M = N$) is indicated by a marker.

Figure 5 shows the valley splitting energies of the L_0, L_1 ground multiplets in conduction (main plot) and valence (inset) bands. One can see that shape and size dependencies, as well as the absolute values of the splittings, are very similar. The maximal splitting energies (solid red line, $M = 0$) decrease as $\approx 1/N^2$ with increase of the lateral size of the NW, while the corresponding band-gap energy scales as $\approx 1/N$. This agrees with previous investigations [27,37]. We note that the rhombic NWs exhibit larger confinement energies than their rectangular counterparts, while the valley mixing in rhombic NWs is strongly suppressed. The same data for the L_2, L_3 ground conduction multiplet are shown in Fig. 6. In the other considered NWs, all the shape and size dependencies of the valley splitting are almost the same.

To justify the robustness of the results, the effects of surface relaxation, passivation, and defects on the valley splittings are considered. The results are summarized in Fig. 7. As an example, the data for the L_0, L_1 conduction band multiplet in anion centered NWs of type Ia are shown.

The first column (0) shows the splitting energies in idealized NWs, the same as shown in Fig. 2, Ia.

The second column (S) shows the effect of few surface layers relaxation. The smooth lines represent continuous shift of the atoms from their ideal bulk towards relaxed positions, taken from Refs. [29,44]. The change of interatomic distances results in the change of transition matrix elements in the tight-binding Hamiltonian, which is taken into account by Harrison's law [30,45].

The third and the fourth columns show the effect of addition (A) and removal (R) of a single atom from the surface of the NW supercell, averaged over all possible defect positions with vertical lines showing the corresponding deviations.

The last column (P) shows the valley splitting in NWs with passivated polar {111} facets. To simulate the passivation, a scheme proposed in Ref. [46] was implemented. To simulate the capping atoms, the *ad hoc* energy ±4 eV [26] was added to the orbital energies extra {111} atomic layers, leaving the bond parameters unchanged.

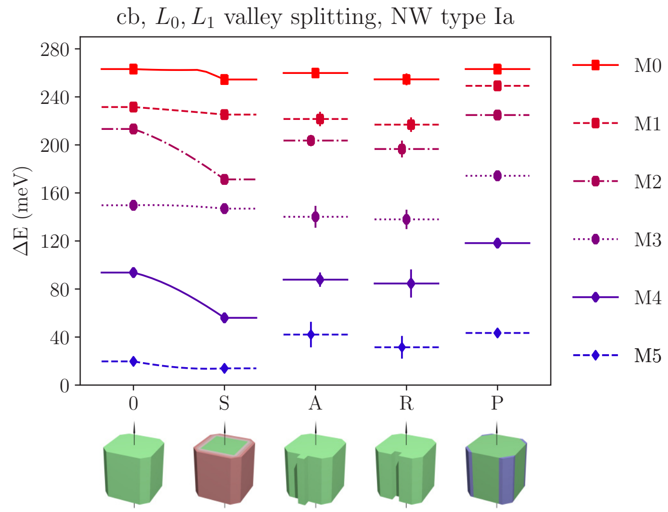

FIG. 7. Effect on the valley splitting of the (S) shift of the NW surface atoms towards relaxed positions, (A) additional atom on the NW surface, (R) removed atom from the NW surface, and (P) passivation of the polar {111} NW facets. The first column (0) shows the splittings in idealized NWs. The corresponding sketches of the NW surface distortions are shown in the bottom. The data are shown for the valley splitting in the conduction band in anion centered NWs (type Ia) with the size parameter $N = 5$.

One can see that the surface defects slightly modify the valley splitting energies, but the main shape dependence holds. These defects have very similar influence on the valley splitting in the valence band and on the splittings in the other NW types. Therefore we conclude that the shape induced suppression of the valley splitting in NWs is rather a physical phenomenon.

IV. CONCLUSION

We studied the valley splitting in [110]-grown nanowires with different size, shape, and symmetry. We demonstrate that the valley splittings substantially depend on the NW shape, for the particular case of prismatic octagonal NWs which is determined by the relative fraction of {001} and {110} facets compared to {111} facets at the NW surface. The values of valley splittings are large, up to 100 meV in NWs about 5 nm in diameter, and scale as $\approx 1/D^2$ on the NW diameter. The splittings tend to have maximal values in rectangular NWs ({001} and {110} facets at the surface) and are almost absent in rhombic NWs (mostly {111} facets at the surface). This result holds for a wide range of NW sizes and different point symmetries and is robust to small surface distortions.

We also found a special type of NWs with nonsymmorphic spatial group, where L_0, L_1 valley multiplets become fourfold degenerate and the splitting of L_2, L_3 multiplets is due to the intervalley coupling via far energy states

Results of this paper, except for the absolute values of the valley splittings, also apply for PbS and PbTe, due to the very similar band structures of these materials.

ACKNOWLEDGMENTS

The author acknowledges fruitful discussions with M. O. Nestoklon and financial support by Russian Foundation for Basic Research Project No. 17-02-00383.

APPENDIX A: MICROSCOPIC WIRE STRUCTURE

PbSe has the rocksalt crystal structure with

$$\boldsymbol{a}_1 = \frac{a}{2}(1, 0, 1),\ \boldsymbol{a}_2 = \frac{a}{2}(1, 1, 0),\ \boldsymbol{a}_3 = \frac{a}{2}(0, 1, 1) \quad \text{(A1)}$$

lattice vectors, where $a = 6.1$ Å is the lattice constant [26]. Reciprocal-lattice vectors are conveniently related with the L valleys 1 as $\boldsymbol{b}_\mu = 2\boldsymbol{k}_\mu$, $\mu = 1, 2, 3$.

With the used tight-binding parametrization [26] the first conduction-band effective mass ratios along the $[\bar{1}10]$, [001], and [110] directions (xyz NW axes) are

$$\frac{m_{0(1)}^{[\bar{1}10]}}{m_{2(3)}^{[\bar{1}10]}} = 0.74, \quad \frac{m_{0(1)}^{[001]}}{m_{2(3)}^{[001]}} = 1, \quad \frac{m_{0(1)}^{[110]}}{m_{2(3)}^{[110]}} = 1.36, \qquad \text{(A2)}$$

where $m_{\mu(\nu)}^{\boldsymbol{n}}$ denotes the effective mass along $\boldsymbol{n}$ of the first conduction-band electron at the $L_{\mu(\nu)}$ valley.

The first three NW types (see Table I) have D_{2h}, C_{2v}, and C_{2v} point groups, respectively. Their symmetries are determined by orientation of C_2 axes and the position of the point symmetry origin relative to the (0,0,0) cation, marked by “x” in Table I. NW type I has an inversion center, three (C_2^x, C_2^y, C_2^z) rotation axes (in the NW coordinates frame), and three corresponding reflection planes $\sigma_v^x, \sigma_v^y, \sigma_h^z$. NW type II has the C_2^x rotation axis and σ_v^y, σ_v^z reflection planes with the point symmetry origin being at $a(-1, 1, 0)/8$. NW type III has the C_2^y rotation axis and σ_v^x, σ_v^z reflection planes with the point symmetry origin being at $a(0, 0, 1)/4$.

NW type IV has a nonsymmorphic spatial group with C_{2h} point symmetry. We use the $a(-1, 1, 2)/8$ point [relative to the (0,0,0) cation] as the point symmetry origin, which results in the following quotient group:

$$\left\{e, a = \left(C_2^z, \frac{\boldsymbol{a}_3}{2}\right), b = \left(\sigma_h^z, \boldsymbol{0}\right), ab = \left(i, \frac{\boldsymbol{a}_3}{2}\right)\right\}. \qquad \text{(A3)}$$

Note that this is not the only possible, but is the most convenient, way to choose the point symmetry origin.

APPENDIX B: SYMMETRY ANALYSIS

Symmetry analysis for the first three NW types is trivial and therefore omitted. Instead, we focus on the NW type IV to describe the absence of the valley splitting in L_0, L_1 valley multiplets.

Following Ref. [47], we use projective representations to classify the states of L_0, L_1 valley multiplets, because these valleys project onto the edge of the NW Brillouin zone. In C_{2h} there are two projective classes: K_0 and K_1. Class K_0 has only one-dimensional (vector and spinor) representations [41], while in K_1 there is only one two-dimensional representation $P^{(1)}$.

Since the L_2, L_3 valleys project onto the Γ point, states of the L_2, L_3 multiplets belong to the class K_0 and can be classified according to Ref. [41]. States of the L_0, L_1 valley multiplets belong to the class K_1, and therefore transform according to $P^{(1)}$. Indeed, the factor system

$$\omega_{\boldsymbol{k}}(g_1, g_2) = e^{i(\boldsymbol{k}-R_1^{-1}\boldsymbol{k})\boldsymbol{\tau}_2} \tag{B1}$$

on elements (A3) with $\boldsymbol{k} = \boldsymbol{k}_0$ or $\boldsymbol{k}_1$, (1), has the form

$$\omega_{\boldsymbol{k}_{0(1)}}(a^k b^p, a^{k'} b^{p'}) = \alpha^{(pk')}, \quad \alpha = -1, \tag{B2}$$

which is the standard form for the class K_1 [47]. Note, since all $\boldsymbol{\tau} \parallel [110]$, the factor system depends only on projection of the wave vector $\boldsymbol{k}$ onto the NW axis.

Next we consider time-reversal symmetry by means of the Herring criterion [47,48], which concerns the relation of ψ and $\hat{T}\psi$, where $\hat{T}$ is the time-reversal operator. The criterion reads as a sum over quotient group

$$\frac{1}{h}\sum_{g\in G/T}\chi(g^2) = \begin{cases} K^2, & (a) \\ 0, & (b), \\ -K^2, & (c) \end{cases} \quad \hat{T}^2 = K^2\hat{I}. \tag{B3}$$

There are three options: ψ and $\hat{T}\psi$ are (a) linearly dependent, (b) linearly independent and transform according to conjugate representations, or (c) equivalent representations. In cases (b) and (c) time-reversal symmetry leads to additional degeneracy of states.

The fact that the factor system for L_0, L_1 multiplets, Eq. (B2), has the standard form allows us to use the explicit form of generator matrices $a = \sigma_z$, $b = \sigma_x$ for $P^{(1)}$ representation from Ref. [47]. With generator matrices the sum (B3) for L_0, L_1 states is easily evaluated,

$$\frac{2 + \mathrm{Tr}\left(\sigma_z^2\right) + \mathrm{Tr}\left(\sigma_x^2\right) - \mathrm{Tr}\left(\sigma_y^2\right)}{4} = 1 = -K^2, \tag{B4}$$

and we see that case (c) is realized. Here $K^2 = -1$ due to the antiunitary nature of time-reversal operator $\hat{T}$ for spinors. Therefore the states of L_0, L_1 multiplets are fourfold degenerate.

Note, for L_2, L_3 states, case (b) is realized, so all the states of L_2, L_3 multiplets are twice degenerate. We also note that evaluation of the sum (B3) in this case is much simpler using the double group approach [41], instead of projective representations theory.

[1] D. V. Talapin and C. B. Murray, PbSe nanocrystal solids for n- and p-channel thin film field-effect transistors, Science **310**, 86 (2005).

[2] D. K. Kim, T. R. Vemulkar, S. J. Oh, W.-K. Koh, C. B. Murray, and C. R. Kagan, Ambipolar and unipolar PbSe nanowire field-effect transistors, ACS Nano **5**, 3230 (2011).

[3] V. Sukhovatkin, S. Hinds, L. Brzozowski, and E. H. Sargent, Colloidal quantum-dot photodetectors exploiting multiexciton generation, Science **324**, 1542 (2009).

[4] L. A. Padilha, G. Nootz, S. Webster, D. J. Hagan, E. W. Van Stryland, L. Levina, V. Sukhovatkin, and E. H. Sargent, Two-photon absorption and multi-exciton generation in lead salt quantum dots, in *Ultrafast Phenomena in Semiconductors and Nanostructure Materials XIV*, edited by Jin-Joo Song, Kong-Thon Tsen, Markus Betz, and Abdulhakem Y. Elezzabi (SPIE, Bellingham, 2010).

[5] F. Gesuele, C. W. Wong, M. Sfeir, W. Kyu Koh, C. B. Murray, and T. Heinz, Ultrafast supercontinuum spectroscopy of multiple exciton states in lead chalcogenide nanorods and nanocrystals, in *Conference on Lasers and Electro-Optics 2012* (Optical Society of America, San Jose, CA, USA, 2012), p. QM2G.2.

[6] N. J. L. K. Davis, M. L. Böhm, M. Tabachnyk, F. Wisnivesky-Rocca-Rivarola, T. C. Jellicoe, C. Ducati, B. Ehrler, and N. C. Greenham, Multiple-exciton generation in lead selenide nanorod solar cells with external quantum efficiencies exceeding 120%, Nat. Commun. **6**, 8259 (2015).

[7] E. Lifshitz, M. Bashouti, V. Kloper, A. Kigel, M. S. Eisen, and S. Berger, Synthesis and characterization of PbSe quantum wires, multipods, quantum rods, and cubes, Nano Lett. **3**, 857 (2003).

[8] K.-S. Cho, D. V. Talapin, W. Gaschler, and C. B. Murray, Designing PbSe nanowires and nanorings through oriented attachment of nanoparticles, J. Am. Chem. Soc. **127**, 7140 (2005).

[9] M. Fardy, A. I. Hochbaum, J. Goldberger, M. M. Zhang, and P. Yang, Synthesis and thermoelectrical characterization of lead chalcogenide nanowires, Adv. Mater. **19**, 3047 (2007).

[10] D. V. Talapin, H. Yu, E. V. Shevchenko, A. Lobo, and C. B. Murray, Synthesis of colloidal PbSe/PbS core-shell nanowires and PbS/Au nanowire-nanocrystal heterostructures, J. Phys. Chem. C **111**, 14049 (2007).

[11] W.-K. Koh, A. C. Bartnik, F. W. Wise, and C. B. Murray, Synthesis of monodisperse PbSe nanorods: A case for oriented attachment, J. Am. Chem. Soc. **132**, 3909 (2010).

[12] J. Akhtar, M. Akhtar, M. A. Malik, P. O'Brien, and J. Raftery, A single-source precursor route to unusual PbSe nanostructures by a solution-liquid-solid method, J. Am. Chem. Soc. **134**, 2485 (2012).

[13] R. Graham and D. Yu, High carrier mobility in single ultrathin colloidal lead selenide nanowire field effect transistors, Nano Lett. **12**, 4360 (2012).

[14] Y.-W. Jun, J.-S. Choi, and J. Cheon, Shape control of semiconductor and metal oxide nanocrystals through nonhydrolytic colloidal routes, Angew. Chem., Int. Ed. Engl. **45**, 3414 (2006).

[15] T. Mokari, M. Zhang, and P. Yang, Shape, size, and assembly control of PbTe nanocrystals, J. Am. Chem. Soc. **129**, 9864 (2007).

[16] A. M. Jawaid, D. J. Asunskis, and P. T. Snee, Shape-controlled colloidal synthesis of rock-salt lead selenide nanocrystals, ACS Nano **5**, 6465 (2011).

[17] D. Placencia, J. E. Boercker, E. E. Foos, and J. G. Tischler, Synthesis and optical properties of PbSe nanorods with controlled diameter and length, J. Phys. Chem. Lett. **6**, 3360 (2015).

[18] S. Y. Jang, Y. M. Song, H. S. Kim, Y. J. Cho, Y. S. Seo, G. B. Jung, C.-W. Lee, J. Park, M. Jung, J. Kim, B. Kim, J.-G. Kim, and Y.-J. Kim, Three synthetic routes to single-crystalline PbS nanowires with controlled growth direction and their electrical transport properties, ACS Nano **4**, 2391 (2010).

[19] J. M. An, A. Franceschetti, and A. Zunger, The excitonic exchange splitting and radiative lifetime in PbSe quantum dots, Nano Lett. **7**, 2129 (2007).

[20] S.-H. Wei and A. Zunger, Electronic and structural anomalies in lead chalcogenides, Phys. Rev. B **55**, 13605 (1997).

[21] A. C. Bartnik, Al. L. Efros, W.-K. Koh, C. B. Murray, and F. W. Wise, Electronic states and optical properties of PbSe nanorods and nanowires, Phys. Rev. B **82**, 195313 (2010).

[22] G. Allan and C. Delerue, Confinement effects in PbSe quantum wells and nanocrystals, Phys. Rev. B **70**, 245321 (2004).

[23] M. O. Nestoklon, L. E. Golub, and E. L. Ivchenko, Spin and valley-orbit splittings in SiGe/Si heterostructures, Phys. Rev. B **73**, 235334 (2006).

[24] J. M. An, A. Franceschetti, S. V. Dudiy, and A. Zunger, The peculiar electronic structure of PbSe quantum dots, Nano Lett. **6**, 2728 (2006).

[25] A. Paul and G. Klimeck, Atomistic study of electronic structure of PbSe nanowires, Appl. Phys. Lett. **98**, 212105 (2011).

[26] A. N. Poddubny, M. O. Nestoklon, and S. V. Goupalov, Anomalous suppression of valley splittings in lead salt nanocrystals without inversion center, Phys. Rev. B **86**, 035324 (2012).

[27] I. D. Avdeev, A. N. Poddubny, S. V. Goupalov, and M. O. Nestoklon, Valley and spin splittings in PbSe nanowires, Phys. Rev. B **96**, 085310 (2017).

[28] M. Argeri, A. Fraccarollo, F. Grassi, L. Marchese, and M. Cossi, Density functional theory modeling of PbSe nanoclusters: Effect of surface passivation on shape and composition, J. Phys. Chem. C **115**, 11382 (2011).

[29] V. L. Deringer and R. Dronskowski, Stabilities and reconstructions of clean PbS and PbSe surfaces: DFT results and the role of dispersion forces, J. Phys. Chem. C **120**, 8813 (2016).

[30] J.-M. Jancu, R. Scholz, F. Beltram, and F. Bassani, Empirical spds* tight-binding calculation for cubic semiconductors: General method and material parameters, Phys. Rev. B **57**, 6493 (1998).

[31] A. N. Poddubny, V. M. Litvyak, M. O. Nestoklon, R. V. Cherbunin, V. V. Golubkov, P. A. Onushchenko, A. N. Babkina, A. A. Onushchenko, and S. V. Goupalov, Role of valley anisotropy in optical absorption of monodisperse PbS nanocrystals, J. Phys. Chem. C **121**, 27766 (2017).

[32] E. O. Wrasse, R. J. Baierle, T. M. Schmidt, and A. Fazzio, Quantum confinement and spin-orbit interactions in PbSe and PbTe nanowires: First-principles calculation, Phys. Rev. B **84**, 245324 (2011).

[33] Y. Liu, D. Kim, O. P. Morris, D. Zhitomirsky, and J. C. Grossman, Origins of the stokes shift in PbS quantum dots: Impact of polydispersity, ligands, and defects, ACS Nano **12**, 2838 (2018).

[34] K. Hummer, A. Grüneis, and G. Kresse, Structural and electronic properties of lead chalcogenides from first principles, Phys. Rev. B **75**, 195211 (2007).

[35] A. Svane, N. E. Christensen, M. Cardona, A. N. Chantis, M. van Schilfgaarde, and T. Kotani, Quasiparticle self-consistent *GW* calculations for PbS, PbSe, and PbTe: Band structure and pressure coefficients, Phys. Rev. B **81**, 245120 (2010).

[36] D. Zherebetskyy, M. Scheele, Y. Zhang, N. Bronstein, C. Thompson, D. Britt, M. Salmeron, P. Alivisatos, and L.-W. Wang, Hydroxylation of the surface of PbS nanocrystals passivated with oleic acid, Science **344**, 1380 (2014).

[37] S. V. Goupalov, Comment on "Electronic structure and optical properties of quantum-confined lead salt nanowires", Phys. Rev. B **84**, 037303 (2011).

[38] I. D. Avdeev and M. O. Nestoklon, Electronic structure of PbSe nanowires, J. Phys.: Conf. Ser. **769**, 012074 (2016).

[39] J. Pawłowski, D. Żebrowski, and S. Bednarek, Valley qubit in a gated **MoS**$_2$ monolayer quantum dot, Phys. Rev. B **97**, 155412 (2018).

[40] P. Yu and M. Cardona, *Fundamentals of Semiconductors: Physics and Materials Properties*, 4th ed. (Springer-Verlag, Berlin, 2010).

[41] G. F. Koster, J. O. Dimmock, R. G. Wheeler, and H. Statz, *The Properties of the Thirty-Two Point Groups* (MIT, Cambridge, MA, 1963).

[42] B. Wang, H. Xia, Z. Zhang, J. Yang, R. Patterson, S. Huang, S. Shrestha, and G. Conibeer, Ab initio calculation of halide ligand passivation on PbSe quantum dot facets, RSC Adv. **6**, 104699 (2016).

[43] M. O. Nestoklon, A. N. Poddubny, P. Voisin, and K. Dohnalova, Tuning optical properties of Ge nanocrystals by Si shell, J. Phys. Chem. C **120**, 18901 (2016).

[44] J. Xin Ma, Y. Jia, Y. Lin Song, E. Jun Liang, L. Ke Wu, F. Wang, X. Chun Wang, and X. Hu, The geometric and electronic properties of the PbS, PbSe and PbTe (001) surfaces, Surf. Sci. **551**, 91 (2004).

[45] W. Harrison, *Electronic Structure and the Properties of Solids: The Physics of the Chemical Bond* (Dover, New York, 1989).

[46] A. N. Poddubny and K. Dohnalová, Direct band gap silicon quantum dots achieved via electronegative capping, Phys. Rev. B **90**, 245439 (2014).

[47] G. L. Bir and G. E. Pikus, *Symmetry and Strain-Induced Effects in Semiconductors* (Wiley, New York, 1974).

[48] C. Herring, Effect of time-reversal symmetry on energy bands of crystals, Phys. Rev. **52**, 361 (1937).